Resonant-Phonon Terahertz Quantum-Cascade Lasers and Video-Rate Terahertz Imaging

Sushil Kumar, *Member, IEEE*, and Alan W. M. Lee, *Member, IEEE*

(Invited Paper)

***Abstract*—We review the development of terahertz quantum-cascade lasers (QCLs) that can be uniquely qualified based on a resonant-phonon depopulation scheme. Record performances in terms of operating temperature and optical power output are reported. The best temperature performance is achieved in the metal–metal (MM) waveguides, which provide near-unity mode confinement and low waveguiding loss at terahertz (THz) frequencies even for cavities with subwavelength dimensions. A pulsed operation up to a heat-sink temperature of 169 K at $\nu \sim 2.7$ THz and a continuous-wave (CW) operation up to 117 K at $\nu \sim 3$ THz are demonstrated with a five-level design that has a two-well injector region. Some of the key temperature degradation mechanisms for this design are discussed. For operation at lower frequencies ($\nu < 2$ THz), a one-well injector design is developed that reduces intersubband absorption losses in the injector region. A QCL operating at $\nu = 1.59$ THz ($\lambda = 188.5$ μm) up to a heat-sink temperature of 71 K in cw mode is demonstrated with that design. To obtain high-power output and low beam divergence from the MM waveguides, a lens-coupled scheme is demonstrated. A peak power output of 145 mW, a beamwidth of 4.8°, and a maximum lasing temperature of 160 K are obtained from a 4.1 THz QCL in this configuration. In the latter part of the paper, we report on the demonstration of video-rate (20 frames/s) terahertz imaging with QCLs as the source for illumination and a 320 × 240 element room-temperature microbolometer focal plane array as the detector. The QCLs for the imaging system are processed into semiinsulating surface-plasmon waveguides, and are operated in a cryogen-free thermomechanical cooler in quasi-CW mode at a heat-sink temperature of ∼30 K. Real-time imaging in transmission mode is demonstrated at a standoff distance of 25 m with a $\nu \sim 4.9$ THz QCL in this setup.**

***Index Terms*—Far-infrared, imaging, intersubband, laser, quantum cascade, real time, resonant phonon, terahertz, video rate.**

I. Introduction

TERAHERTZ (THz) ($\nu \sim 1$–10 THz, $\lambda \sim 30$–300 μm) frequencies are among the least explored of the electromagnetic spectrum mainly due to the lack of suitable sources of coherent radiation. A multitude of applications exist for terahertz spectroscopy, sensing, and imaging: be it in astronomy for identification of interstellar molecular species, remote sensing and monitoring of earth's atmosphere, biomedical imaging, detection of concealed weapons and drugs, end-point detection in plasma-etching processes, etc. [1].[1],[2] For imaging applications [2], THz radiation is specifically useful, since many materials such as paper, plastics, and ceramics, which are opaque to visible frequencies, are transmissive at longer wavelengths. In comparison to microwaves, THz radiation provides a better spatial resolution due to its shorter wavelength. When compared to imaging with the high-energy X-rays, THz imaging is noninvasive and can provide much better contrast in terms of identification of different materials due to their largely different absorption and refraction indexes across the THz spectrum.

Even though sensitive THz detectors have long existed [3], there has been a dearth of compact solid-state THz sources that could provide large (>1 mW) radiation intensities in a continuous-wave (CW) operation. The output power from electronic sources such as transistors, Gunn oscillators, Schottky-diode frequency multipliers typically falls to microwatts levels for $\nu > 1$ THz. Sources such as photomixers and parametric oscillators that utilize optical down-conversion to generate THz radiation also have low average power. In comparison, THz quantum-cascade lasers (QCLs) [4] now provide a CW spectral coverage from $\nu \sim 1.2$ THz [5] through $\nu \sim 5$ THz (in cryogenic operation), with optical power output in the tens of milliwatts range, and are poised to become one of the most important types of THz radiation source [6].

A QCL [7] emits photons due to unipolar intersubband transitions in the quantum wells (QWs) of a semiconductor heterostructure. It is often cited as the foremost example of "bandgap engineering," since the energy spacing between the radiative levels can be artificially engineered by varying the thickness of the epitaxially grown QWs. The past decade has witnessed remarkable progress in the development of the mid-infrared (IR) ($\lambda \sim 3$–30 μm) QCLs [8], and room-temperature CW operation has been demonstrated for $\lambda \sim 5$–10 μm QCLs grown by both molecular beam epitaxy (MBE) and metal organic vapor-phase epitaxy (MOVPE) techniques [9]–[11]. In contrast, the invention of the THz QCLs has relatively been more recent, and there is still a lot to be desired in their development, the foremost being the operation at temperatures accessible by the present day thermoelectric coolers (>∼220 K).

Manuscript received October 3, 2007; revised December 24, 2007. This work was supported in part by the Air Force Office of Scientific Research (AFOSR), in part by the National Aeronautics and Space Administration (NASA), and in part by the National Science Foundation (NSF).

S. Kumar is with the Research Laboratory of Electronics, Massachusetts Institute of Technology, Cambridge, MA 02139 USA (e-mail: sushil@mit.edu).

Alan W. M. Lee is with the Department of Electrical Engineering and Computer Science, Massachusetts Institute of Technology, Cambridge, MA 02139 USA (e-mail: awmlee@mit.edu).

Color versions of one or more of the figures in this paper are available online at http://ieeexplore.ieee.org.

Digital Object Identifier 10.1109/JSTQE.2007.915510

[1]The terahertz gap: The generation of far-infrared radiation and its applications, *Phil. Trans. Roy. Soc. London A,* vol. 362, no. 1815, 2004 (special issue with a compilation of 15 papers).

[2]Photonic terahertz technology, *Semicond. Sci. Technol.,* vol. 20, no. 7, 2005 (special issue with a compilation of 22 papers).

In this paper, we review THz QCLs with active regions based on a characteristic *resonant-phonon* depopulation scheme [12], [13] as opposed to the superlattice [4] or bound-to-continuum [14] based designs. The first part of the paper is devoted to the active region design principles and experimental results from different designs. Some of the main temperature degradation mechanisms in resonant-phonon THz QCLs are discussed. The latter part of the paper focuses more on the practical applications aspect of these lasers, and discusses some of the video-rate imaging experiments that have been performed with the QCLs.

The waveguide design for THz QCLs merits a comprehensive treatment in itself [15]; thus, any related discussion will be kept to a minimum in this paper. Two types of waveguides have so far been utilized for THz QCLs: the semiinsulating surface-plasmon (SISP) waveguides [4] and the metal–metal (MM) waveguides [16]. The latter have demonstrated the best temperature performance owing to their lower loss and almost unity mode confinement at THz frequencies. However, edge-emitting MM waveguides suffer from divergent output beams [17] and low-out-coupling efficiency [15]. The usable optical power output and also the beam quality of the MM ridge lasers can be significantly enhanced by abutting a silicon hyperhemispherical lens to the cleaved facets for ridge lasers as will be shown in Section VI. It may be noted that distributed feedback gratings have been implemented with the MM waveguides to obtain robust single-mode emission [18] and also better beam patterns via surface emission [19], [20], but such structures will not be discussed in the present context.

II. Challenges in the Active Region Design of a THz QCL

Light amplification in semiconductor superlattices was proposed as early as 1971 by the mechanism of photon-assisted resonant tunneling (RT) through a potential barrier [22]. Although RT through a double barrier was observed soon afterward [23], it took another decade before the sequential RT could be observed in a semiconductor superlattice [24]. This was partly due to the implicit difficulty in electrically biasing a semiconductor superlattice due to the occurrence of negative differential resistance (NDR) regions in its current–voltage (I–V) characteristics that disrupted the electric field across the structure by the formation of high-field domains [25]. The successful demonstration of the first superlattice-based intersubband laser (i.e., the QCL) was in large part due to the development of an *injector* region [7], which limits the current flow in the structure at low bias, and allows the population inversion to be established between the radiative levels as the applied bias is increased toward the "design" bias. This prevents the superlattice from being biased through an NDR region to reach the operating condition on its I–V characteristics.

Fig. 1 shows one of the simplest representative three-level THz QCL designs. At the design bias [Fig. 1(a)], electrons are transported from the injector level $1'$ into the upper radiative level 3 by an RT through the injector barrier A. A subpicosecond lifetime is maintained for the lower radiative level 2 by making E_{21} resonant with the longitudinal optical (LO) phonon energy $\hbar\omega_{\rm LO}$ (≈36 meV in GaAs) to allow fast electron-LO-phonon

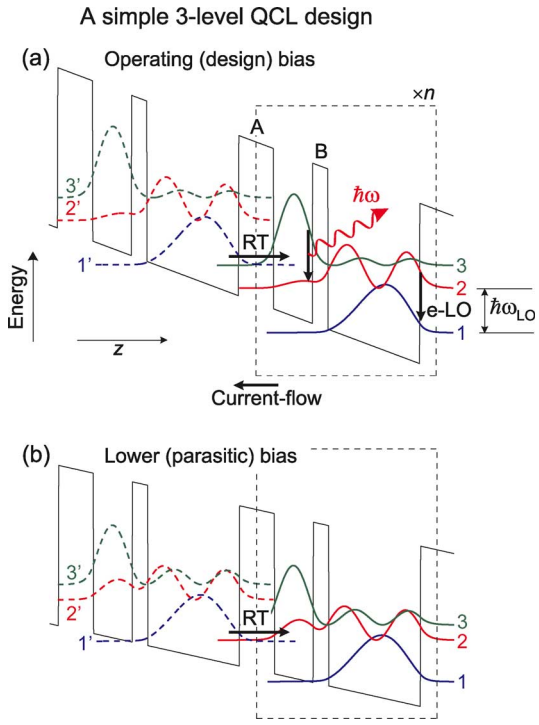

Fig. 1. Conduction band diagram showing two modules of a representative simple three-level QCL structure with an LO-phonon-assisted depopulation scheme. (a) At "design" bias (b) At "parasitic" bias.. Moduli-squared wavefunctions are vertically displaced in the QWs according to their energies. Levels 3 and 2 are the radiative levels and level 1 is the "injector" level. Electron transport through the injector barrier A is primarily by the mechanism of RT [21].

scattering from $3 \rightarrow 2$. A minimum of two QWs per module are required to independently set E_{21}, the radiative energy E_{32}, and the radiative dipole matrix element z_{32} ($\equiv \langle 3|\hat{z}|2\rangle$). Assuming a Lorentzian lineshape for the $3 \rightarrow 2$ radiative transition with a full-width at half-maximum (FWHM) linewidth of $\Delta\nu$ centered at a frequency $\nu = \nu_{32} \equiv (E_3 - E_2)/(2\pi\hbar)$, the expression for the peak gain (per unit length) reads (in per centimeters)

$$g = \frac{e^2}{2\pi m^* \epsilon_0 n_{\rm r} c}\frac{\Delta n_{32} f_{32}}{\Delta\nu} \overset{\rm GaAs}{\approx} 70\frac{[\Delta n_{32}/(10^{15}\ {\rm cm}^{-3})]f_{32}}{[\Delta\nu/(1\ {\rm THz})]} \quad (1)$$

where Δn_{32} is the three-dimensional inverted population density, $f_{32} = (4\pi m^* \nu_{32} z_{32}^2)/\hbar$ is the unitless oscillator strength, m^* is the conduction band effective mass and $n_{\rm r}$ is the refractive index of the material. Assuming unity injection efficiency for RT from $1' \rightarrow 3$, an inversion density

$$\Delta n_{32} = \frac{J}{eL_{\rm mod}}\tau_3\left(1 - \frac{\tau_2}{\tau_{32}}\right) \quad (2)$$

is established for a current density J (current per unit surface area) flowing through the structure, where $L_{\rm mod}$ is the length of one QCL module, e is the unit electronic charge, and the (non-radiative) scattering times are averaged over all the electrons in a given subband.

The simple model design of Fig. 1 and (1) and (2) could provide an insight into the challenges for THz QCL design. For polar materials such as GaAs or InGaAs, LO-phonon emission

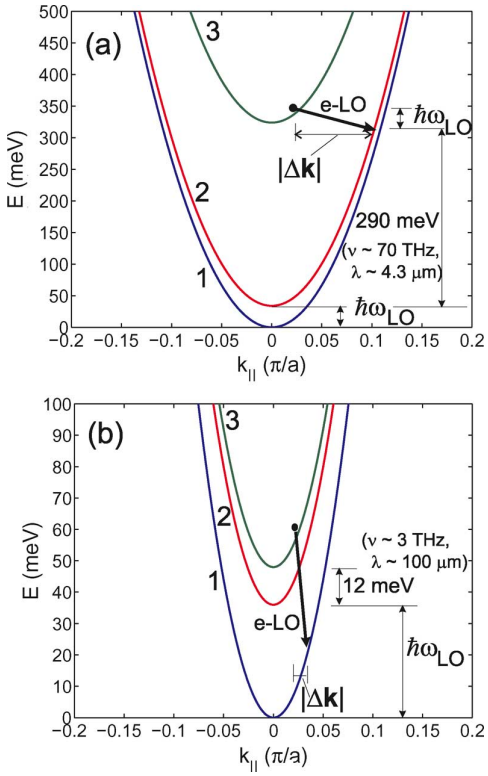

Fig. 2. Typical energy spacings and in-plane (parabolic) subband dispersion for the three-level structure of Fig. 1 corresponding to the following. (a) Mid-IR QCL (InGaAs/InAlAs). (b) THz QCL (GaAs/AlGaAs). $k_{\|}$ is the in-plane wave vector plotted in units of π/a, where a is the lattice constant.

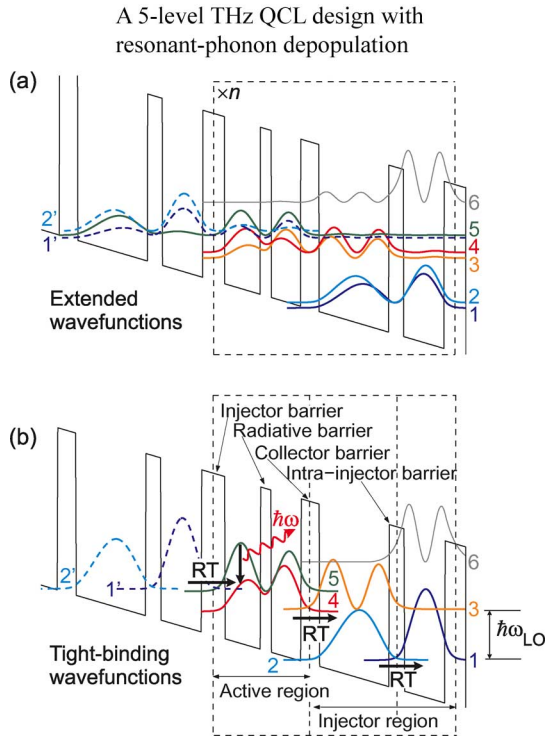

Fig. 3. Conductionband diagram for a five-level THz QCL design in the GaAs/$Al_{0.15}Ga_{0.85}As$ material system ($\hbar\omega_{LO} \sim 36$ meV, barrier height ~135 meV) calculated at the design bias. (a) In extended scheme (using the potential profile as shown). (b) Tight-binding scheme (with one QCL module further divided into three submodules as marked).

is the dominant energy relaxation mechanism for the electrons, and the matrix element for the scattering rate is $\propto 1/|\Delta \boldsymbol{k}|$, where $|\Delta \boldsymbol{k}|$ is the momentum exchanged in the scattering process [26]. The energy spacing for mid-IR QCLs is such that $E_{32} \gg \hbar\omega_{\mathrm{LO}}$, whereby the momentum exchange involved for an electron-LO-phonon scattering event from level $3 \rightarrow (2, 1)$ is an order of magnitude greater than it is from level $2 \rightarrow 1$, which is apparent from Fig. 2(a). Consequently, $\tau_{\mathrm{e-LO}}$ from level $3 \rightarrow 2, 1$ (~2–5 ps) is an order of magnitude larger than that from level $2 \rightarrow 1$ (~0.2–0.5 ps). A large population inversion could thus be established between the radiative levels 3 and 2. In contrast, maintaining a long lifetime for the upper level 3 is considerably more difficult in a THz QCL due to the small value of $|\Delta \boldsymbol{k}|$ involved, as seen in Fig. 2(b).

The dynamic range of lasing in current for a QCL critically depends on the design of the injector region. The RT transport through the injector barrier is ideally kept coherent by making the injector barrier thin, such that the peak operating current J_{peak} is dictated by the upper level lifetime rather than the barrier thickness [21]. For THz QCLs, however, the $1' \rightarrow 3$ transport cannot be made too coherent to limit the parasitic current conduction at low bias that happens for the level alignment analogous to that in Fig. 1(b). If the injector barrier is made too transparent, the current conducted at the $1' \rightarrow 2$ alignment can exceed that of the $1' \rightarrow 3$ alignment at the design bias, which causes an early NDR in the I–V characteristics, thereby preventing operation at the design bias. Even if an early NDR is avoided, a coherent injection mechanism is accompanied by a large anticrossing energy splitting between levels $1'$ and 3 that will reduce the $1' \rightarrow 3$ injection efficiency, and thus, the population inversion density. This is caused by $1' \rightarrow 2$ leakage at the operating bias condition due to the small energy spacing between the radiative levels at THz frequencies. In comparison, mid-IR QCLs do not suffer from the problem of large low-bias parasitic conduction, since the parasitic alignment happens much earlier to the design bias due to a large E_{32}, at which point the subbands reside deep in the QWs rendering any intermodule coupling between them negligible.

III. Resonant-Phonon Depopulation Scheme

Based on just the momentum exchange involved in the LO-phonon emission process, the nonradiative lifetimes in a THz QCL design that utilizes the LO-phonon-assisted depopulation will approximately be the same for both the radiative levels as discussed in the previous section. In this situation, a longer upper level lifetime can be obtained for the design in Fig. 1 by making the radiative transition from $3 \rightarrow 2$ spatially diagonal, which reduces the spatial overlap between levels 3 and 1 and limits the $3 \rightarrow 1$ scattering. This, however, comes at the cost of a reduced dipole matrix element z_{32}, and consequently, a smaller peak gain, as is evident from equation (1). (Note that, at low temperatures, electron-LO-phonon scattering from $3 \rightarrow 2$ is energetically forbidden; this is discussed further in Section IV-A.)

The three-level design of Fig. 1 can be radically improved by introducing two additional QWs per module, and correspondingly, two additional subbands that take part in

the electrical transport. Such a modified five-level design is shown in Fig. 3(a). This was the first THz QCL design to have explicitly utilized an LO-phonon-scattering-assisted depopulation scheme [12]. The operation of this design is better understood when the wavefunctions are recalculated in the tight-binding scheme of Fig. 3(b). Of the two main modifications to the three-level design, the primary one is in the depopulation mechanism. The lower radiative level 4, instead of being directly depopulated, is designed to be in resonance with another level 3 that has a very short lifetime (∼0.2 ps). The depopulation is thus a two-step process that includes $4 \rightarrow 3$ *RT* and $3 \rightarrow 2$ electron-LO-*phonon* scattering. The main benefit from this *resonant-phonon* depopulation mechanism is that the $5 \rightarrow 4$ radiative transition could be designed to be spatially vertical to allow for a large dipole matrix element, while still maintaining a long lifetime for the upper radiative level 5, since $5 \rightarrow (2, 1)$ scattering is negligible due to the spatial delocalization, and $5 \rightarrow 3$ tunneling is inefficient due to a relatively large energy detuning from the 5–3 resonance condition. A second important feature of the five-level design is the two-well injector region. Below the design bias the injector levels 1 and 2 are energetically detuned from their resonance alignment, which prevents the low-bias parasitic current flow in the structure and allows for a better dynamic range in current for lasing.

A. Experimental Results for the Five-Level Design

Each of the four potential barriers in the five-level design play a critical role in its operation. The thicknesses of the injector, collector, and the intrainjector barriers controls the nature of the corresponding RT transport (coherent or incoherent [21]), and the thickness of the radiative barrier determines the 4–5 anticrossing splitting Δ_{45}, and thus, the radiative energy E_{54}. The radiative levels 4 and 5 could be designed to be off-resonance at the design bias by adjusting the width of the wells in the active region such that $E_{54} > \Delta_{45}$ (which, however, reduces the oscillator strength f_{54} from its maximum possible value at resonance). The width of the QWs in the injector region could be adjusted to change the alignment of the aforementioned RT transitions with respect to each other.

THz QCLs operating in the range of $\nu \sim 2.1$ THz [30] to $\nu \sim 5$ THz [29] have so far been demonstrated with this design. In context of the tight-binding wavefunctions of Fig. 3(b), the optimum performance for designs operating at $\nu \gtrsim 2.5$ THz has been obtained by designing the aforementioned RT alignments to be concurrently at resonance at the *design bias* (i.e., the bias corresponding to the $1'$–5 resonance), and with the following typical values for the anticrossing energies: $\Delta_{12} \sim \Delta_{34} \sim 4$ meV and $\Delta_{1'5} \sim 3$ meV. The design becomes more challenging at lower frequencies since the low-bias parasitic couplings [similar to that in Fig. 1(b)] get enhanced due to a smaller difference in the bias fields required for the design and the parasitic bias alignments, respectively.

Fig. 4 shows the design details and experimental results in pulsed operation for a 2.7 THz QCL labeled FL178C-M10 ($\nu \sim 2.7$ THz, wafer EA1252 with 178 QCL modules, growth details similar to those in [27]). The value of $T_{\max,\mathrm{pul}} \sim 169$ K for this

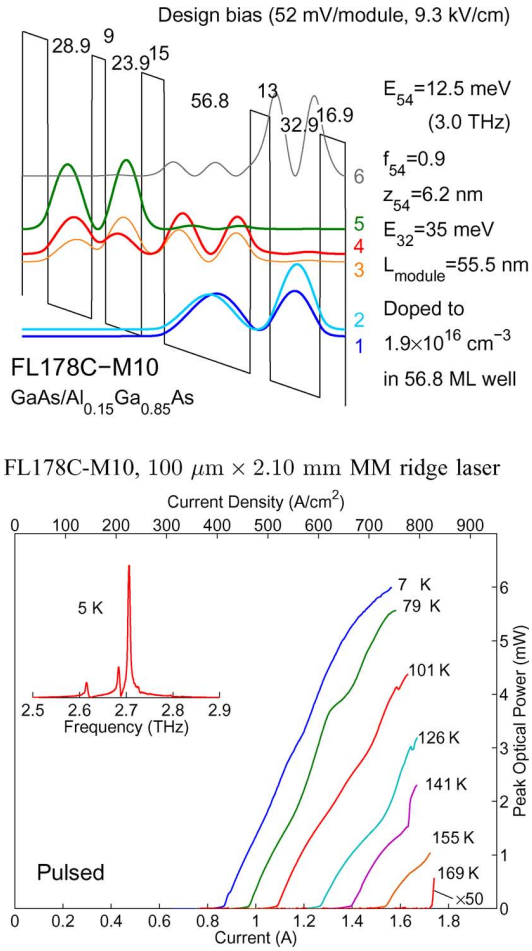

Fig. 4. Single-moduleconduction band diagram at design bias (top) and pulsed measurement results (bottom) for a 2.7 THz QCL with the five-level active region design of Fig. 3. The layer thicknesses are reported in the units of a monolayer (1 ML = 2.825 Å) on top of the wells and barriers in addition to other design details on the band diagram. The wafer was processed into MM ridge waveguides by a Cu–Cu thermocompression wafer-bonding technique and dry etching [27]. The ridge lasers with cleaved open ended facets were biased with 200 ns pulses repeated at 10 kHz. Light was collected with a Winston cone placed adjacent to the laser facet. Optical power versus current (L–I) curves at different heat-sink temperatures were measured with a liquid-Helium-cooled Ge:Ga photodetector. The detected optical power was calibrated with a thermopile power meter (ScienTech, model AC2500). The representative spectrum in the inset at the bottom was measured with a Nicolet 850 spectrometer and the Ge:Gaphotodetector.

design is presently the record high-temperature performance for any THz QCL.

MM ridge lasers could be made very narrow without significantly increasing the waveguide losses owing to the strong mode confinement in the MM waveguides even at subwavelength dimensions. Narrow ridges have efficient lateral heat removal, and hence, provide better CW performance without the need of any complex fabrication techniques. Moreover, rear facet highreflectivity (HR) coatings are not needed due to inherent large facet reflectivities in the MM waveguides at THz frequencies ($R \sim 0.7$–0.9) [15], thus eliminating one of the dominant failure mechanisms of the lasers in a repeated CW operation. Fig. 5 shows CW measurement results from a narrow ridge $\nu \sim 3$ THz QCL with a similar five-level design that achieved a record high-CW operating temperature of 117 K

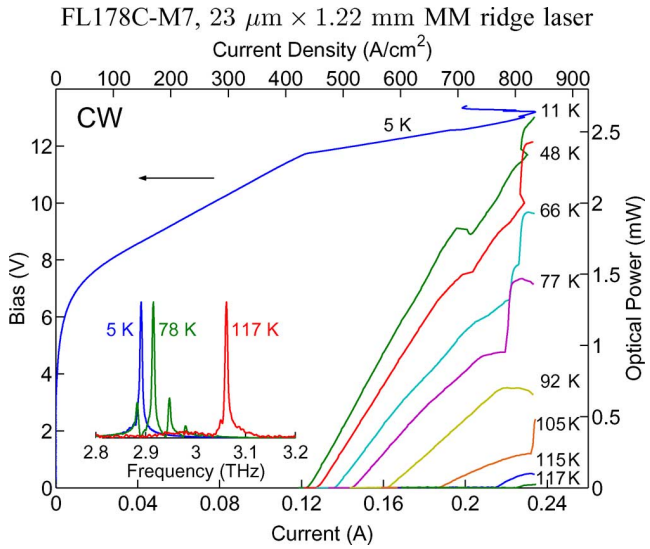

Fig. 5. CW L–Is versus heat-sink temperature for a $\nu \sim 3$ THz QCL [27]. The QCL design, labeled as FL178C-M7 (wafer EA1121), and the fabrication procedure are very similar to that of the FL178C-M10 laser shown in Fig. 4. The semiconductor substrate was lapped down to a thickness of 170 μm to improve heat sinking. The L–Is were recorded using a room-temperature pyroelectric detector (Molectron, model P4-42), and the spectra were measured using a Nicolet 850 spectrometer with a room-temperature deuterated triglycine sulfate (DTGS) pyroelectric detector. Absolute power measurements were done similarly to that described in the caption of Fig. 4. This device lased up to 158 K in pulsed mode.

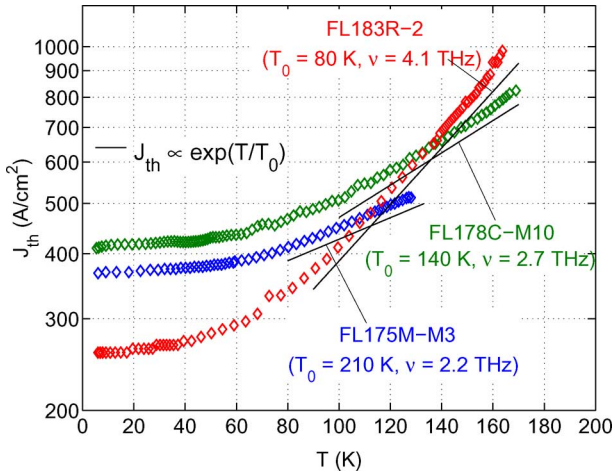

Fig. 6. Semilogarithmicplot of the $J_{\rm th}$–T variation in the pulsed operation for three different THz QCLs fabricated with the MM (Cu–Cu) waveguides based on the five-level design of Fig. 3. A phenomenological fit of the high-T data points to the expression $J_{\rm th} \propto \exp(T/T_0)$ is also indicated, where T is the heat-sink temperature. The FL175M-M3 ($\nu \sim 2.2$ THz) design is similar to the FL178C-M10 design, but with a 11 ML thick radiative barrier, and the corresponding results are from a 75 μm × 0.64 mm ridge device that had a value of $T_{\rm max,pul} \sim 128$ K. Similarly the FL183R-2 ($\nu \sim 4.1$ THz) design is with a 6 ML thick radiative barrier, and the corresponding results are from a 80 μm × 1.94 mm ridge device that had a value of $T_{\rm max,pul} \sim 165$ K (see also Fig. 12).

[27]. It is also worth nothing that microcavity THz QCLs with subwavelength mode volumes have recently been demonstrated in the MM waveguides to obtain lasers with ultralow electrical power consumption [30], [31].

IV. Temperature Degradation Mechanisms

Fig. 6 captures the threshold current density ($J_{\rm th}$) versus the heat-sink temperature (T) variation for QCLs operating at different frequencies. The dynamic range in lasing current ($J_{\rm peak}/J_{\rm th,5\,K}$) reduces at lower frequencies due to stronger low-bias parasitic couplings, but so does the rate of increase of $J_{\rm th}$ with T. Consequently, the maximum operating temperature is similar for the 2.7 THz ($T_{\rm max,pul} \sim 169$ K) and the 4.1 THz ($T_{\rm max,pul} \sim 165$ K) designs, respectively. However, at frequencies below 2.5 THz, the low-bias parasitic current channels tend to limit the dynamic range severely. Note that the $J_{\rm peak}$ for the five-level design remains approximately the same at all temperatures up to the maximum lasing temperature for a given design (this can be seen more clearly in Fig. 9).

The high-T data points in the $J_{\rm th}$–T variation can typically be fit to a phenomenological expression $J_{\rm th} \propto \exp(T/T_0)$. Although no physical mechanism has yet been identified to explain such a relation, the expression works remarkably well for several different types of QCL designs at a wide range of frequencies (including the mid-IR QCLs). Thus, the characteristic temperature T_0 and the lasing dynamic range $J_{\rm peak}/J_{\rm th,5\,K}$ are often used to compare temperature performances of different designs. This section describes some of the main possible temperature degradation mechanisms in the resonant-phonon designs that may explain the observed experimental behavior.

A. Thermally Activated LO-Phonon Scattering

One of the primary temperature degradation mechanisms in THz QCLs with LO-phonon-scattering-assisted depopulation is believed to be the reduction in the lifetime of the upper radiative level (u) due to thermally activated LO-phonon scattering from that level to the lower radiative level (l). This is because the radiative energy separation $E_{ul} < \hbar\omega_{\rm LO}$ for THz QCLs, and hence, only the electrons in the level u with kinetic energy $E(k_\parallel)$ ($=\hbar^2 k_\parallel^2/2m^*$) that is greater than $\hbar\omega_{\rm LO} - E_{ul}$ can scatter into the lower level l by emitting an LO-phonon. The dependence of the LO-phonon scattering rate on the electron wave vector $\boldsymbol{k}_\parallel$ is weak. Hence, the lifetime $\tau_{ul,\rm LO}$ due to the LO-phonon emission from the level $u \rightarrow l$ can be approximately expressed as

$$\tau_{ul,\rm LO} \approx \tau_{ul,\rm LO}^{\rm hot} \exp\left(\frac{T_1}{T_{\rm e}}\right) \tag{3}$$

where

$$T_1 \equiv \frac{\hbar\omega_{\rm LO} - E_{ul}}{k_{\rm B}}. \tag{4}$$

The previous expression neglects state-blocking in the level l. $T_{\rm e}$ is the characteristic temperature for the electronic distribution in level u that is assumed to be Maxwell–Boltzmann like, $\tau_{ul,\rm LO}^{\rm hot}$ is the scattering time for the electrons with kinetic energy $E(k_{\parallel,\rm LO}) = \hbar\omega_{\rm LO} - E_{ul}$, which is the lowest kinetic energy in level u for which such a scattering is possible, and $\exp(T_1/T_{\rm e})$ is the fraction of the electrons that have a kinetic energy greater than $E(k_{\parallel,\rm LO})$. The variable $\tau_{ul,\rm LO}^{\rm hot}$ can be calculated analytically [32], and is a function of the overlap of the electron wavefunctions and the momentum of the LO-phonons that can be

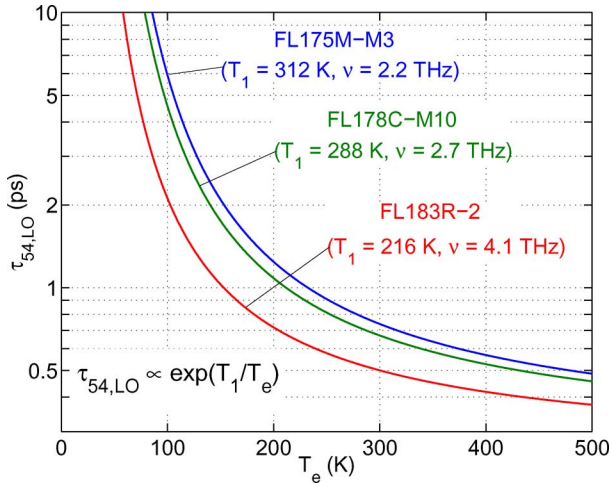

Fig. 7. Semilogarithmicplot of the $\tau_{54,\mathrm{LO}}$-T_e variation for three different five-level designs with E_{54} [$\sim \hbar\omega$, Fig. 3(b)] values of 9.1, 11.2, and 17.0 meV corresponding to frequencies of 2.2, 2.7, and 4.1 THz, respectively. The value $\tau_{54,\mathrm{LO}}^{\mathrm{hot}}$ is calculated to be ~ 0.25 ps for all the three designs, and (3) is used for the plots with $\hbar\omega_{\mathrm{LO}} \sim 36$ meV corresponding to the value in bulk GaAs. Here, T_e is the electronic temperature that characterizes the thermal (Maxwell–Boltzmann like) distribution of the electrons in the upper radiative level 5.

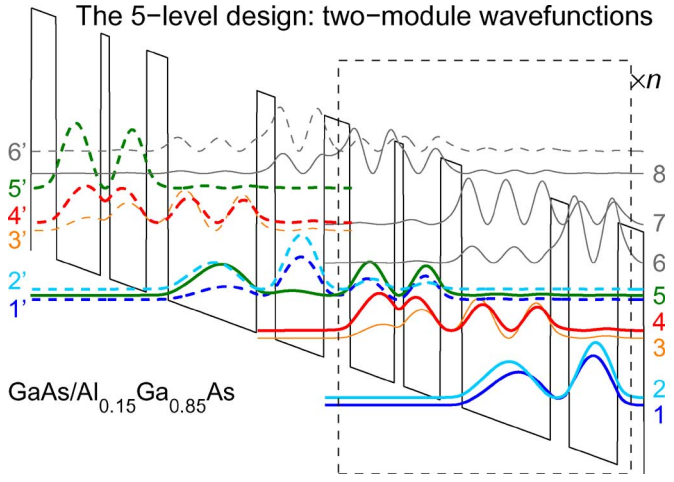

Fig. 8. Two-module conduction band diagram for the five-level design of Fig. 3(a) calculated at the design bias. In addition to levels 1–5 that take active part in the transport, the higher energy excited levels 6–8 may also contribute to the parasitic current conduction close to the design bias alignment.

emitted. T_e increases with the heat-sink temperature T although it is a highly nontrivial problem to estimate its value. Numerical simulations as well as some experimental measurements predict T_e to be 50–100 K higher than the lattice temperature during the device operation [33]–[35].

The reduction in the lifetime of the upper radiative level $\tau_{54,\mathrm{LO}}$ with the electronic temperature T_e for THz QCLs based on the five-level design of Fig. 3 and operating at three different frequencies is shown in Fig. 7. Even though the $\tau_{54,\mathrm{LO}}$-T variation in Fig. 7 might qualitatively explain the J_{th}–T variation in Fig. 6 (since the population inversion, and hence, the gain diminishes with a reduced lifetime of the upper radiative level), it is not quite consistent quantitatively. Note that $\tau_{54,\mathrm{LO}} \propto \exp(T_1/T_\mathrm{e})$, whereas $J_{\mathrm{th}} \propto \exp(T/T_0)$ as a phenomenological fit to the experimental results. First, both these expressions have a different dependence on the temperature in the exponent, which is difficult to explain mathematically for any algebraic relation between J_{th} and $\tau_{54,\mathrm{LO}}$. Second, the $\tau_{54,\mathrm{LO}}$–T variation for the FL175M-M3 design in Fig. 7 is not considerably different from that of the FL178C-M10 design, as is also apparent from their similar T_1 values. However, these two designs have largely different T_0 values, as seen from Fig. 6. Clearly then, some other complex temperature degradation mechanisms are also at play.

B. Parasitic Leakage Current and Level Broadening

In the simplest case, the tunneling probability through a potential barrier is considered independent of the in-plane wave vector of the electron $k_\parallel$, as in the original model proposed by Esaki and Tsu [36]. However, in the most general case, the in-plane and the z-directed electron motion gets coupled in a heterostructure due to interband-mixing effects and interface-roughness, which makes the tunneling $k_\parallel$-dependent [37]. With an increased temperature, the electrons in a subband acquire larger values for $k_\parallel$ that may lead to tunneling into parasitic levels that are otherwise energetically detuned from the resonance. Fig. 8 shows a two-module conduction band diagram for the five-level design. Due to the close proximity of the upper radiative level $5'$ with the low-lying upper excited level 8 in the adjacent module, thermally activated $5' \rightarrow 8$ tunneling is likely to reduce the lifetime of level $5'$, and therefore, the population inversion with increasing temperature, given that the $5' - 8$ interaction is relatively strong (the anticrossing energy $\Delta_{5'8} > \sim$1 meV). Taking band non-parabolicity into account within an energy dependent effective mass model [38], $E_{85'}$ is calculated to be $\sim$19, 14.5, and 7.5 meV for the FL175M-M3, FL178C-M10, and FL183R-2 designs, respectively. The relatively large energy separation for FL175M-M3 could possibly explain the relatively weak J_{th}–T variation for this design in Fig. 6.

The electronic subbands are likely to become energetically broadened at higher temperatures due to increased scattering. For example, the work presented in [39] predicts an increased impurity scattering due to ineffective screening of the impurity potential by the thermally energetic electrons as the primary mechanism for such broadening. The peak gain in the structure will decrease due to a broader radiative linewidth. Additionally, broader subbands lead to poorer injection efficiency into the upper radiative level close to the design bias, and also strengthen the low-bias parasitic current channels, which would artificially increase J_{th}, thereby pinching off the dynamic range of lasing in current. A typical experimental measurement of the I–Vs and the R–Is for the five-level design is shown in Fig. 9 (where $\mathcal{R} = dV/dI$ is the differential resistance). The kink in the I–V around $\sim$12 V and the corresponding discontinuity in $\mathcal{R}$ are indicative of the onset of lasing [21]. It is evident that the current increases at low-bias conditions even though the peak current density near the operating bias region does not change significantly, which could be due to the aforementioned increase in the low-bias parasitic current conduction. The low-bias valleys in the R–I plot at 5 K, believed to be due to the $2' \rightarrow 3$ and the $1' \rightarrow 3$

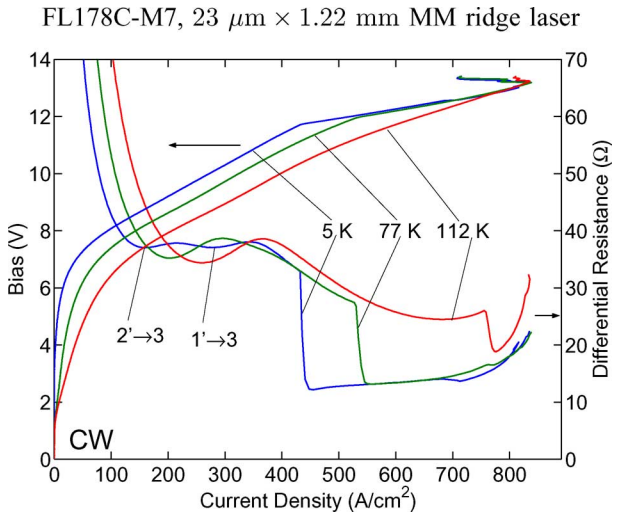

Fig. 9. Variation of the I–Vs and the R–Is ($\mathcal{R} \equiv dV/dI$) with the heat-sink temperature $T_{\rm cw}$ in the CW operation for the same laser as in Fig. 5. The lattice temperature T in the CW operation is likely to be T sim $T_{\rm cw}$ + (50–70) K (deduced from the values of $T_{\rm max,pul} = 158$ K and $T_{\rm max,cw} = 117$ K for this device, and the fact that the active region is hotter than the heat-sink by 20–30 K even during the short-pulsed operation).

alignment, respectively, also disappear at higher temperatures likely due to level broadening.

V. One-Well Injector Design for Low-Frequency ($\nu < 2$ THz) Operation

The operation of THz QCLs at frequencies below 2 THz is desired partly due to the attractiveness of this region of spectrum for THz imaging over long distances due to some of the very transparent atmospheric transmission windows that exist in the spectral range of 1–1.5 THz. Also, many materials such as clothing become increasingly transparent in the low THz frequency range, which makes this part of the spectrum ideal for security-based imaging applications. There is also a broad interest in astronomy, for example, to observe the fine structure lines of singly ionized nitrogen at $\nu = 1.46$ THz and carbon at $\nu = 1.90$ THz to understand the structure and evolution of the Universe.

The lowest frequency laser obtained with the five-level design in Section III has two injector levels operated at $\nu \sim 2.1$ THz [28]. The operation at lower frequencies in designs with multiple injector levels is challenged by the optical losses that are induced due to the intersubband absorption within the injector region. This happens because the intersubband energy separation in the injector becomes comparable to the photon energy for $\nu <$ ~2 THz ($\hbar\omega \lesssim 8$ meV). Also, the injection selectivity into the upper radiative level for such a design suffers, since the energy separation between the radiative levels becomes similar to that of the injector levels.

By designing a "tightly anticrossed" ($\Delta_{12} \ll \hbar\omega$) doublet of injector levels, the operation down to $\nu \sim 1.2$ THz has already been demonstrated in design with two injector levels and a miniband-based extraction scheme [5]. Our approach to obtain low-frequency operation is an active region design based on a one-well injector scheme with resonant-phonon depopulation [41]. The intersubband dipole selection rule in QCLs precludes the electric field from coupling directly to the in-plane electron motion. Since most of the carriers reside in the injector region, the lack of additional subbands in a one-well injector is likely to prevent reabsorption of the THz photons due to intersubband transitions in the injector region. This is in contrast to very-low-frequency QCLs that have been demonstrated by using strong magnetic fields applied perpendicular to the layers, which increases the modal gain by increasing the lifetime of the upper radiative level, and decreases the free carrier absorption in the structure by in-plane localization of the carriers and subsequent quenching of the intersubband scattering channels [42].

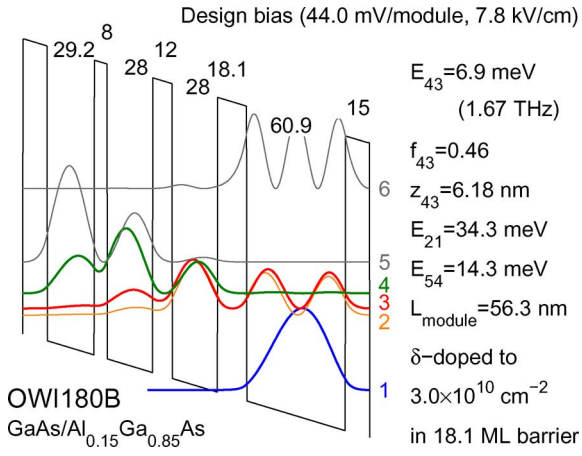

Fig. 10. Single-module conduction band diagram of a $\nu \sim 1.6$ THz one-well injector design at the design bias [42]. The radiative transition is from level $4 \rightarrow 3$. At low temperatures, only four of the lowest energy subbands take active part in the electronic transport. The layer thicknesses are indicated on the top of the wells and the barriers in the units of 1 ML.

Fig. 10 shows the single-module conduction band diagram for a $\nu \sim 1.6$ THz one-well injector design labeled as OWI180B [40]. The primary challenge in this design is to minimize the low-bias parasitic current channels (predominantly due to $1' \rightarrow$ 2 coupling), which can cause premature occurrence of a NDR region, as discussed in Section II. This is achieved by adding an extra well to the active region (as compared to the five-level design of Fig. 3) to spatially extend the upper radiative level, and thus, increase the radiative oscillator strength for a given low-bias parasitic $1'$–2 coupling.

Experimental results for an OWI180B MM ridge laser are shown in Fig. 11. The lasing range $J_{\rm max}/J_{\rm th,5\ K}$ for this design is very small due to a strong low-bias parasitic current channel. Nevertheless, this device lased up to a value of $T_{\rm max,cw} \sim 71$ K, and more than 0.65 mW of optical power was detected with a thermopile detector in the CW operation. An improved active region that minimizes the low-bias parasitic couplings by making the radiative transition more diagonal is expected to obtain a more robust operation at even lower frequencies for this design.

VI. Lens Coupled MM Waveguide QCLs

Both SISP and MM waveguides have features that are advantageous for imaging: devices based on SISP waveguides have been observed with power levels an order of magnitude larger than those based on MM waveguides, with narrow beam patterns

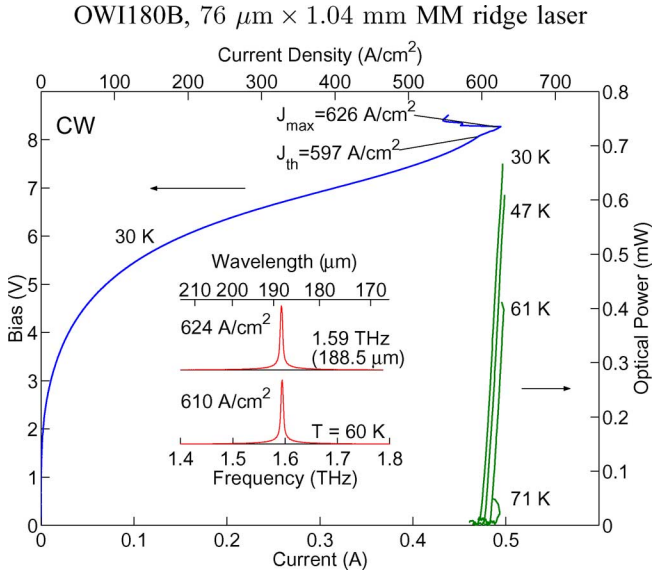

Fig. 11. Experimental results in the CW operation for an MM (Cu–Cu) ridge laser for the OWI180B design (wafer V0416 grown with 180 repeated QCL modules). The growth and fabrication details are similar to those in [41].

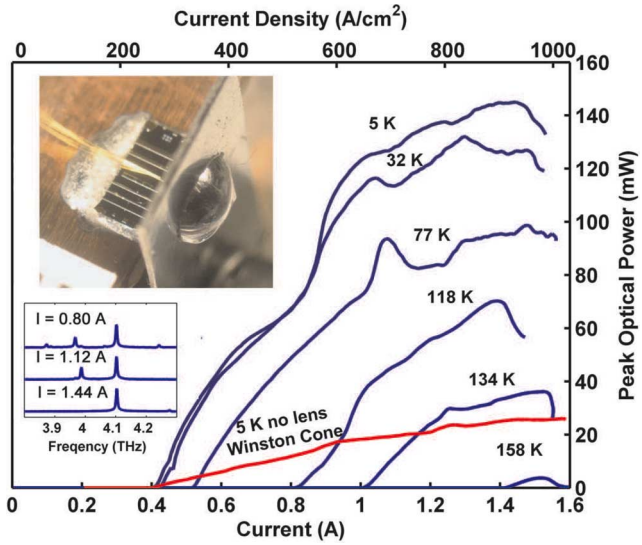

Fig. 12. Peak pulsed optical power against current for 80-μm-wide, 1.96-mm-long MM waveguide QCL with coupled lens (at various temperatures) and without coupled lens (at 5 K). Upper inset shows image of lens-coupled MM QCL. Lower inset shows typical spectra for lens-coupled device. The active region of this device is described in [43]. This device was processed into wet-etched MM ridge waveguides using the same etch-chemistry as in [20].

[4], [43], [44], allowing the illumination of multiple pixels [45], or fast raster scanning in imaging [46]; MM-waveguide-based devices have demonstrated the highest operating temperatures (Section III-A). Prior works have improved beam patterns and output powers of MM devices through the use of surface emission [20] or the use of an integrated horn antenna [47]; however, these techniques required a modification of the waveguide structure. A different approach is described here: a lens is abutted to the output facet of an unmodified MM waveguide that increases the radiation in the forward direction and forms a narrow beam while lowering the reflectivity [48]. These effects increase the collected output power and improve the beam pattern of a conventional MM waveguide while retaining the high-temperature performance.

A full discussion of the parameters affecting the power, beam shape, and maximum operating temperature of MM and SISP waveguides is given in [15]. However, the waveguide properties largely result form the differences in confinement factors (Γ)—the overlap of the optical mode with the active region—of MM and SISP waveguides. The SISP waveguide has a low Γ ($\sim$ 0.1–0.5), and the majority of the mode extends into the undoped substrate, making the transverse spatial extent of the optical mode on the order of λ_0 (freespace wavelength, typically 60–300 μm). This results in a planewave-like reflectivity ($R \sim 0.32$, mirror loss $\alpha_m \sim 10\ \mathrm{cm}^{-1}$) at the GaAs/Air output facet, and also in a low divergence beam that is efficiently collected (i.e., high collection efficiency, η). The MM waveguide has a near-unity confinement factor ($\Gamma \approx 1$), resulting from the closely spaced top and bottom metal strips (10 μm height in our devices), which confine the mode to the active region [15]. The narrow spacing is much less than λ_0, resulting in nearly isotropic beam patterns that are difficult to collect [17], [49], and enhanced reflectivity (0.6–0.9, α_m of 0.5–3 cm^{-1}). As a results, MM waveguides have low values of apparent power slope efficiency: $dP/dI \propto \eta\alpha_m/(\alpha_w + \alpha_m)$ (in watts per ampere), where α_w is the waveguide loss that is much larger than α_m. SISP devices have larger α_m, with α_m and α_w in a better relative balance, and exhibit higher powers. For example, comparably sized FL183R-2 devices fabricated from the same wafer in SISP and MM waveguides have produced 248 mW [43] and 26 mW (Fig. 12), respectively. However, the same devices lased up to heat-sink temperatures of 105 and 165 K in SISP and MM, respectively. This large temperature difference results from differences in the threshold gain (g_{th}), which must equal the total losses of the waveguide divided by the modal overlap: $g_{\mathrm{th}} = (\alpha_w + \alpha_m)/\Gamma$. At elevated temperatures where the gain is reduced, low α_m and high Γ of MM waveguides contribute to lower g_{th}, while for SISP waveguides, the larger values of α_m and α_w (likely caused by impurities in the semiinsulating substrate) along with low Γ contribute to higher threshold gain. To improve the measured power of an MM waveguide, while retaining its temperature performance, increases can be made to η or, to a lesser extent, α_m.

To improve the beam pattern and reduce the reflectivity of the output mirror of an edge-emitting FL183R-2 (same active region as the one in [43]) MM ridge laser, a high-resistivity silicon (HRSi) spacer was abutted to the output facet (Fig. 12). The dielectric is nearly index matched to the GaAs active region (nGaAs $\sim$ 3.6 compared with nSi $\sim$ 3.4), reducing the reflectivity, while the presence of the HRSi dielectric increases the radiation in the forward (spacer) direction, similar to planar antenna structures fabricated on thick dielectric substrates, widely used in a time-domain THz spectroscopy [50]. A hyperhemispherical lens placed on the backside of the spacer is used to increase the directivity further. The radius of the lens is chosen to be 1.5 mm in order to minimize absorption losses, while still having the Si/air boundary in the far field, $>20\ \lambda_0$ at the 4.1 THz lasing frequency. The total length of the lens is 1.62 mm,

making the total setback (sb) from the center 0.46 mm, roughly at the R/n aplanatic point [50]. By increasing the setback length, the divergence of the emitted rays can be further reduced, at the expense of a larger fraction of the marginal rays undergoing total internal reflection at the lens boundary. To reduce internal reflections, the lens was antireflection coated using a $\sim$14-μm-thick layer of low-density polyethylene (LDPE, with $n \approx 1.5$) that acts as a quarter-wave impedance matching layer.

The results for a lens-coupled MM device ($\sim$80 μm wide, 1.96 mm long) show marked improvement in emitted power over the same device tested without a lens by using only a Winston cone for collection (Fig. 12). For the lens-coupled device, at 5 K, in pulsed mode (200 ns 1% duty-cycle), the maximum peak power was 145 mW, lasing up to a heat-sink temperature of 160 K, with a threshold current density of $J_{\rm th} = 266$ A/cm^2 and a wall-plug power efficiency of 0.7%. The Winston cone-coupled device produced 26 mW, and lased up to 165 K, with $J_{\rm th} = 254$ A/cm^2 (Fig. 12). The decrease in temperature with the use of the lens is consistent with an increased $g_{\rm th}$ caused by increased α_m. This is also true for the small increase in $J_{\rm th}$, which increases with $g_{\rm th}$ in devices based on the resonant-phonon active region. However, these effects are relatively small when compared with an SISP device fabricated from the same wafer (98 μm wide, 2.15 mm long) that had a threshold current density of 530 A/cm^2 at 5 K, and a much lower maximum pulsed operating temperature of 105 K [43]. The overall losses $(\alpha_m + \alpha_w)/\Gamma$ of the MM waveguide devices are not yet approaching those of the SISP devices, and α_m could be increased further allowing an improvement in the output power.

The decrease in the maximum operating temperature and an increase in $J_{\rm th}$ are small in scale compared to the SISP device, suggesting that the decreased reflectivity is a minor effect. Furthermore, large variations in power were observed for similarly sized devices depending on the positioning of the spacer, and it was suspected that small air gaps might exist between the facet and the spacer. To model this effect, finite-element simulations of the reflectivity versus the gap distance were performed using a geometry similar to that in [15]. The reflectivity is plotted against this air gap distance for the fundamental and first two even-symmetry lateral modes (Fig. 13). At larger gap distances, the effect of the spacer is reduced, and the reflectivity of the fundamental mode approaches 74%, which is the open facet reflectivity calculated in [15]. At the zero gap distance, the facet reflectivity is reduced below 10% due to the elimination of dielectric mismatch, and the reduction of the wavelength outside the cavity $\lambda_0/n_{\rm Si}$, which eases modal mismatch. Scanning-electron microscope (SEM) images of various MM waveguide facets revealed micrometer-scale protrusions resulting from tearing of the top and bottom metal strips during cleaving. Thus, small gaps are unavoidable for facets that are defined by cleaving, and act to limit the reduction in reflectivity.

A larger effect on the enhancement of power is expected from improved collection efficiency by the presence of the dielectric. For antennas fabricated on thick, high $\epsilon_{\rm r}$ substrates, the ratio power radiated into air and the substrate is roughly $1{:}\epsilon_{\rm r}^{3/2}$ for slot and dipole antennas [50], and a similar effect is expected

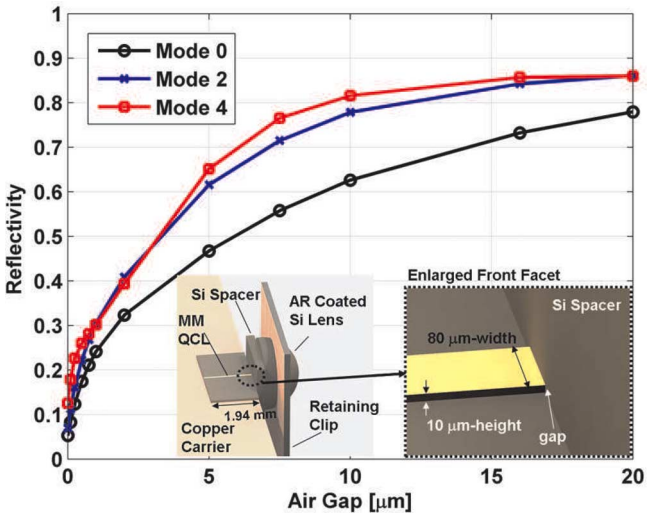

Fig. 13. Output facet reflectivity of an MM waveguide (80 μm wide and 10 μm high) with a high-resistivity Si spacer placed at various air gap distances.

with the spacer-covered facet. Using finite element simulations to model the radiation patterns of the bare and covered facets, the improvement in collection efficiency between the lens-coupled and bare-faceted devices for the fundamental lateral mode was calculated to be 16$\times$ [48]. The observed improvement in power between the lens and the Winston cone, and the Winston cone and bare facet are 5.5$\times$ and 4.3$\times$, respectively, giving an overall improvement of the 23$\times$ for the lens over the bare facet. This improvement factor includes the effects of collection efficiency and decreased reflectivity, and was in a relatively good agreement with the numerical results.

The FWHM of the beam was measured to be 4.8°. This allows nearly all of the emitted power to be collected in an $f/1$ optic, external to the cryogenic dewar, whereas $\sim$85% of the power can be collected by using the SISP device and even less with a bare-faceted MM device. This large amount of collected power allows the flood illumination of microbolometer arrays or the use of a spatial filter to improve the beam, which is useful for coupling to single-mode antennas used in heterodyne detectors. In both cases, a high average power is essential. The lens-coupled MM device was tested at 25% duty cycle where it produced 102 mW with 2-μs-long pulses. A device fabricated from a different wafer (FL179C-M9-2, lasing frequency at $\sim$2.7 THz, 80 μm wide, 1.2 mm long) was tested in MM configuration yielding $\sim$50 mW of CW power at 30 K in a closed-cycle cryorefrigerator. This high-CW power at 30 K is better than the performance of the larger FL183R-2 SISP device at this temperature [50], demonstrating the benefits of this technique.

The lens-coupled MM device has combined the key features of both SISP and MM waveguides: it produced a peak power of 145 mW, within a factor of 2 of the highest power QCL, with a maximum operating temperature of 160 K, which is $<$10 K below the highest demonstrated operating temperature (Fig. 4), while maintaining a narrow beamwidth of 4.8°. Future improvement of the lens-coupling should improve optical powers even further.

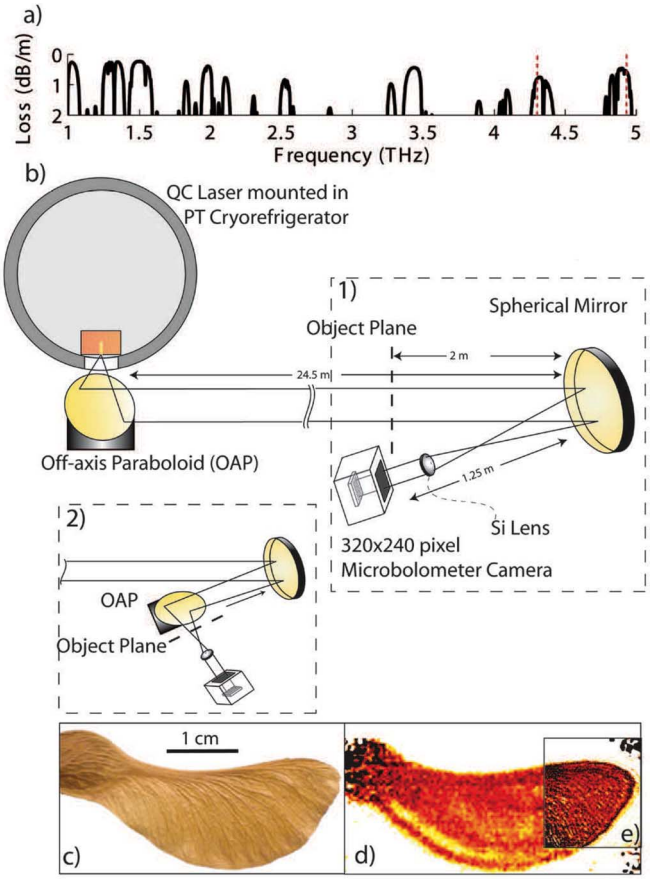

Fig. 14. (a) Atmospheric path loss. (b) Experimental setup of the THz imaging system over 25 m distance. (c) Image of seed pod (visible). (d) and (e) Configurations (1) and (2), respectively.

VII. Long-Distance and Video-Rate THz Imaging

The use of THz radiation for nondestructive evaluation has been proposed for various pharmaceutical [51], industrial [52] and security applications [53]. Imaging at THz frequencies is attractive because of the nonionizing photon energies and the spectral features that exist at these frequencies [2]. Additionally, the high optical transparency of many common packaging materials along with the reasonable spatial resolutions allow the possibility of practical inspection systems. In these applications, the single-pixel raster scanning techniques used with time-domain THz sources and QCLs [46] might prove prohibitive, as acquisition times for a single high-resolution image can be several minutes. For these purposes, the high powers of QCLs can be used to advantage in real time (~30 frames per second) imaging when used to illuminate microbolometer arrays (Fig. 14) [45]. The use of narrowband QCLs also allows the transmission over longer distances in the atmosphere, as their frequencies can be designed for the narrow atmospheric water windows, shown in Fig. 14, which are less than a few hundred gigahertz wide. This is demonstrated with the combination of high-power QCL and broadband multielement detector imaging over a distance of 25 m using the setup shown in Fig. 14 [45]. The QCL is cooled to ~33 K by a closed-cycle pulsed-tube cryorefrigerator, allowing cryogen-free operation. For imaging over the 25 m path length, a

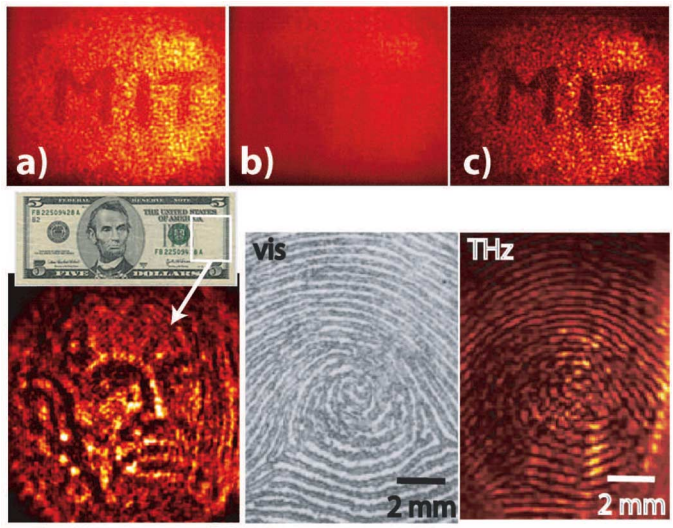

Fig. 15. Three frame differential imaging sequence (a)–(c). (a) Frame 1 with THz superimposed on infrared signal. (b) Frame 3 with infrared signal and a small amount of residual THz signal. (c) Difference between frames 1 and 3, resulting in THz only signal, showing the absorption of pencil on paper. (d) and (e) THz image of watermark in the transmission mode and THz image of fingerprint in the reflection mode, respectively.

4.9 THz SISP QCL was chosen based on the relative balance of the high optical power (~17 mW) and position within a low-loss atmospheric window (0.52 dB/m at 294 K and 48% RH). The resulting images demonstrate the ability to do real-time imaging over this path length (SNR ~10, 1 s integration time). At frequencies outside the atmospheric windows (4.9 ± 0.2 THz), the absorption increases significantly (>10 dB/m), illustrating the importance of frequency selection in THz sources. The use of a broadband THz source in this case would result in large losses of transmitted power.

The camera used for this demonstration was an unmodified commercially produced microbolometer array. The camera is an uncooled 320×240 element array based on thin-film vanadium oxide (VO_x) bolometer resistors (model SCC500, BAE Systems, Lexington, MA) [**?**]. The thin-film resistors are deposited on a silicon nitride airbridge, which together acts as the radiation absorber. This structure is suspended over a reflecting backplane, forming a highly absorbent, resonant optical cavity in the 7.5–14 μm [long wavelength infrared (LWIR)] night vision band. The low heat capacity of the 46.25 μm pitch elements result in a thermal time constant $\tau \approx 13$ms, allowing a 60 Hz frame rate. At 4.3 and 4.9 THz, the bolometers are calculated to have absorptions of 4% and 6%, respectively, due to the reduced absorption of the materials and the shorting effect of the reflecting backplane at the longer wavelengths (61 and 70 μm).

In the transmission mode setup, the use of the array at THz frequencies results in a THz image superimposed on a strong infrared background [Fig. 15(a)]. In order to allow the subtraction of the infrared background, the QCL is biased synchronously with the first (signal) frame of a three-frame sequence. Due to the thermal time constant, some residual THz signal remains, and the second frame is discarded (not shown). The third (reference) frame (b) is used as the infrared background and is subtracted from the first frame, resulting in a THz only image (c). This

differential imaging scheme obviates the need for infrared blocking filters with an additional benefit of suppressing $1/f$ noise, which increases with integration time without the differential scheme. The penalty for using this scheme is a reduction in the frame rate to 20 Hz; however, this rate is still sufficient for real-time imaging applications.

The sensitivity of the camera was characterized at 4.3 THz in differential mode, where the responsivity was measured to be 8.1×10^6 counts/W with an rms noise of $\sigma \approx 2.6$ counts/$\sqrt{\text{Hz}}$. The resulting optical noise equivalent power was $\text{NEP}_0 \approx 320$ pw/$\sqrt{\text{Hz}}$ that is substantially higher than the electrical noise equivalent power (NEP_E) of 0.9 pW/$\sqrt{\text{Hz}}$. This large reduction in sensitivity can be attributed to the low absorption at 4.3 THz (4%), the low transmission through the Ge camera window (38%), and the microbolometer thermal time constant limiting the temperature rise to $\sim$42% of the peak value. The NEP_0 equates to a noise equivalent delta temperature (NEDT) of $\sim$40 K, assuming a predetection bandwidth of 10% and a diffraction-limited beam. This is substantially higher than the infrared NEDT of 40 mK, therefore passive imaging at THz frequencies would require a high temperature contrast, a strong infrared blocking filter, and long integration times that would include increasing amounts of $1/f$ noise.

The microbolometer array is sensitive enough to provide an SNR of $\sim$340 when illuminated by the $\sim$50 mW, 4.3 THz QCL (Fig. 15). Here, the SNR is an averaged over the 80×10^3 element array, and is naturally much higher at the center where the beam is strongest. To maximize the overall signal, reflective optics were used to guide the beam to the object because of their low losses. For the imaging optic, an $f/1$ HRSi meniscus lens was used because of its high $n_{\text{Si}} \sim 3.4$ and low losses (< 1 cm^{-1}). The combination of high n_{Si} and meniscus shape allow the thickness of the lens to be minimized. Similar to the lens-coupled work, a coating of LDPE was used as an antireflection layer. Fig. 15 shows a single frame in transmission through the watermark on a five-dollar bill, demonstrating high speed (1/20 s acquisition time) with good SNR. The THz image of the finger print was taken in reflection mode by flattening the print against a sheet of LDPE to provide a specular surface for 20-frame average image. The images of Fig. 15 show relatively high resolutions of $<$500 μm, which are to be expected from the 70 μm wavelength and the fast silicon optic.

The combination of the high-power QCL and an infrared microbolometer array has allowed video-rate imaging, with SNRs of 25 dB, despite the poor THz absorption by the microbolometer elements. Two orders of magnitude of improvement should be possible by the optimization of the microbolometer camera, which should allow a greater penetration of packaging materials and imaging of diffuse reflected THz radiation in a potential application as an inspection system. An ideal system would combine the broadband detectors with various QCLs tailored to atmospheric windows, allowing a spectroscopic analysis.

ACKNOWLEDGMENT

The authors would like to thank Q. Hu, B. S. Williams, H. Callebaut, Q. Qin, J. L. Reno, Z. Wasilewski, and H. C. Liu for their contributions to the work described here. Sandia is a multiprogram laboratory operated by Sandia Corporation, a Lockheed Martin Company, for the U.S. Department of Energy under Contract DE-AC04-94AL85000.

REFERENCES

[1] P. H. Siegel, "Terahertz technology," *IEEE Trans. Microw. Theory Tech.*, vol. 50, no. 3, pp. 910–928, Mar. 2002.

[2] W. L. Chan, J. Diebel, and D. M. Mittleman, "Imaging with terahertz radiation," *Rep. Prog. Phys.*, vol. 70, pp. 1325–1379, 2007.

[3] E. E. Haller, "Advanced far-infrared detectors," *Infrared Phys.*, vol. 35, pp. 127–146, 1994.

[4] R. Köhler, A. Tredicucci, F. Beltram, H. E. Beere, E. H. Linfield, A. G. Davies, D. A. Ritchie, R. C. Iotti, and F. Rossi, "Terahertz semiconductor-heterostructure laser," *Nature*, vol. 417, pp. 156–159, 2002.

[5] C. Walther, M. Fischer, G. Scalari, R. Terazzi, N. Hoyler, and J. Faist, "Quantum cascade lasers operating from 1.2 to 1.6 THz," *Appl. Phys. Lett.*, vol. 91, pp. 131122-1–131122-3, 2007.

[6] B. S. Williams, "Terahertz quantum-cascade lasers," *Nat. Photon.*, vol. 1, pp. 517–525, 2007.

[7] J. Faist, F. Capasso, D. L. Sivco, C. Sirtori, A. L. Hutchinson, and A. Y. Cho, "Quantum cascade laser," *Science*, vol. 264, pp. 553–556, 1994.

[8] C. Gmachl, F. Capasso, D. L. Sivco, and A. Y. Cho, "Recent progress in quantum cascade lasers and applications," *Rep. Prog. Phys.*, vol. 64, pp. 1533–1601, 2001.

[9] M. Beck, D. Hofstetter, T. Aellen, J. Faist, U. Oesterle, M. Ilegems, E. Gini, and H. Melchior, "Continuous wave operation of a mid-infrared semiconductor laser at room temperature," *Science*, vol. 295, p. 301, 2002.

[10] L. Diehl, D. Bour, S. Corzine, J. Zhu, G. Hfler, M. Lonar, M. Troccoli, and F. Capasso, "High-power quantum cascade lasers grown by low-pressure metal organic vapor-phase epitaxy operating in continuous wave above 400 K," *Appl. Phys. Lett.*, vol. 88, p. 201115, 2006.

[11] A. Evans, S. R. Darvish, S. Slivken, Y. Bai, and M. Razeghi, "Buried heterostructure quantum cascade lasers with high continuous-wave wall plug efficiency," *Appl. Phys. Lett.*, vol. 91, p. 071101, 2007.

[12] B. S. Williams, H. Callebaut, S. Kumar, Q. Hu, and J. L. Reno, "3.4-THz quantum cascade laser based on longitudinal-optical-phonon scattering for depopulation," *Appl. Phys. Lett.*, vol. 82, p. 1015, 2003.

[13] Q. Hu, B. S. Williams, S. Kumar, H. Callebaut, S. Kohen, and J. L. Reno, "Resonant-phonon-assisted THz quantum-cascade lasers with metal–metal waveguides," *Semicond. Sci. Technol.*, vol. 20, p. S228, 2005.

[14] G. Scalari, L. Ajili, J. Faist, H. Beere, E. Linfield, D. Ritchie, and G. Davies, "Far-infrared ($\lambda \cong 87$ μm) bound-to-continuum quantum- cascade lasers operating up to 90 K," *Appl. Phys. Lett.*, vol. 82, p. 3165, 2003.

[15] S. Kohen, B. S. Williams, and Q. Hu, "Electromagnetic modeling of terahertz quantum cascade laser waveguides and resonators," *J. Appl. Phys.*, vol. 97, p. 053106, 2005.

[16] B. S. Williams, S. Kumar, H. Callebaut, Q. Hu, and J. L. Reno, "Terahertz quantum-cascade laser at $\lambda \approx 100$ μm using metal waveguide for mode confinement," *Appl. Phys. Lett.*, vol. 83, p. 2124, 2003.

[17] A. J. L. Adam, I. KaŠalynas,, J. N. Hovenier, T. O. Klaassen, J. R. Gao, E. E. Orlova, B. S. Williams, S. Kumar, Q. Hu, and J. L. Reno, "Beam patterns of terahertz quantum cascade lasers with subwavelength cavity dimensions," *Appl. Phys. Lett.*, vol. 88, p. 151105, 2006.

[18] B. S. Williams, S. Kumar, Q. Hu, and J. L. Reno, "Distributed-feedback terahertz quantum-cascade lasers with laterally corrugated metal waveguides," *Opt. Lett.*, vol. 30, p. 2909, 2005.

[19] J. A. Fan, M. A. Belkin, F. Capasso, S. Khanna, M. Lachab, A. G. Davies, and E. H. Linfield, "Surface emitting terahertz quantum cascade laser with a double–metal waveguide," *Opt. Exp.*, vol. 14, p. 11672, 2007.

[20] S. Kumar, B. S. Williams, Q. Qin, A. W. M. Lee, Q. Hu, and J. L. Reno, "Surface-emitting distributed feedback terahertz quantum-cascade lasers in metaln–metal waveguides," *Opt. Exp.*, vol. 15, p. 113, 2007.

[21] C. Sirtori, F. Capasso, J. Faist, A. L. Hutchinson, D. L. Sivco, and A. Y. Cho, "Resonant tunneling in quantum cascade lasers," *IEEE J. Quantum Electron.*, vol. 34, p. 1722, 1998.

[22] R. F. Kazarinov and R. A. Suris, "Possibility of the amplification of electromagnetic waves in a semiconductor with a superlattice," *Sov. Phys. Semicond.*, vol. 5, p. 707, 1971.

[23] L. L. Chang, L. Esaki, and R. Tsu, "Resonant tunneling in semiconductor double barriers," *Appl. Phys. Lett.*, vol. 24, p. 593, 1974.
[24] F. Capasso, K. Mohammed, and A. Y. Cho, "Sequential resonant tunneling through a multiquantum-well superlattice," *Appl. Phys. Lett.*, vol. 48, p. 478, 1986.
[25] L. L. Bonilla and H. T. Grahn, "Non-linear dynamics of semiconductor superlattices," *Rep. Prog. Phys.*, vol. 68, pp. 577–683, 2005.
[26] J. Faist, F. Capasso, C. Sirtori, D. L. Sivco, and A. Y. Cho, "Quantum cascade lasers," in *Intersubband Transitions in Quantum Wells: Physics and Device Applications II,* vol. 66, eser. Semiconductor and Semimetals, H. C. Liu and F. Capasso, Eds. San Diego, CA: Academic, 2000.
[27] B. S. Williams, S. Kumar, Q. Hu, and J. L. Reno, "Operation of terahertz quantum-cascade lasers at 164 K in pulsed mode and at 117 K in continuous-wave mode," *Opt. Exp.*, vol. 13, p. 3331, 2005.
[28] B. S. Williams, S. Kumar, Q. Hu, and J. L. Reno, "Resonant-phonon terahertz quantum-cascade laser operating at 2.1 THz ($\lambda \cong 141\ \mu$m)," *Electron. Lett.*, vol. 40, p. 431, 2004.
[29] A. Lee, Q. Qin, S. Kumar, B. S. Williams, Q. Hu, and J. L. Reno, "Real-time terahertz imaging over a standoff distance (>25 m)," *Appl. Phys. Lett.*, vol. 89, p. 141125, 2006.
[30] Y. Chassagneux, J. Palomo, R. Colombelli, S. Dhillon, C. Sirtori, H. Beere, J. Alton, and D. Ritchie, "Terahertz microcavity lasers with subwavelength mode volumes and thresholds in the milliampere range," *Appl. Phys. Lett.*, vol. 90, p. 091113, 2007.
[31] L. A. Dunbar, R. Houdré, G. Scalari, L. Sirigu, M. Giovannini, and J. Faist, "Small optical volume terahertz emitting microdisk quantum cascade lasers," *Appl. Phys. Lett.*, vol. 90, p. 141114, 2007.
[32] J. H. Smet, C. G. Fonstad, and Q. Hu, "Intrawell and interwell intersubband transitions in multiple quantum wells for far-infrared sources," *J. Appl. Phys.*, vol. 79, p. 9305, 1996.
[33] H. Callebaut, S. Kumar, B. S. Williams, Q. Hu, and J. L. Reno, "Importance of electron-impurity scattering for electron transport in terahertz quantum-cascade lasers," *Appl. Phys. Lett.*, vol. 84, p. 645, 2004.
[34] H. Callebaut and Q. Hu, "Importance of coherence for electron transport in terahertz quantum cascade lasers," *J. Appl. Phys.*, vol. 98, p. 104505, 2005.
[35] M. S. Vitiello, G. Scamarcio, V. Spagnolo, B. S. Williams, S. Kumar, Q. Hu, and J. L. Reno, "Measurement of subband electronic temperatures and population inversion in THz quantum-cascade lasers," *Appl. Phys. Lett.*, vol. 86, p. 111115, 2005.
[36] L. Esaki and R. Tsu, "Tunneling in a finite superlattice," *Appl. Phys. Lett.*, vol. 22, p. 562, 1973.
[37] T. B. Boykin, R. E. Carnahan, and K. P. Martin, "Inadequacy of the one-dimensional approximation for resonant-tunneling-diode current-voltage calculations," *Phys. Rev. B*, vol. 51, p. 2273, 1995.
[38] R. P. Leavitt, "Empirical two-band model for quantum wells and superlattices in an electric field," *Phys. Rev. B*, vol. 44, p. 11270, 1991.
[39] R. Nelander and A. Wacker, "The effects of temperature on the gain profile of THz quantum cascade lasers," presented at the 9th Int. Conf. Intersubband Transitions Quantum Wells, Ambleside, Cumbria, U.K., Sep. 10–14 2007.
[40] S. Kumar, Q. Qin, B. S. Williams, Q. Hu, Z. R. Wasilewski, X. Wu, and H. C. Liu, "Quantum-cascade lasers with one-well injector operating at 1.59 THz ($\lambda = 188.5\ \mu$m)," presented at the Lasers Electro-Opt. Conf., Baltimore, MD, May 6–11 2007.
[41] S. Kumar, B. S. Williams, Q. Hu, and J. L. Reno, "1.9 THz quantum-cascade lasers with one-well injector," *Appl. Phys. Lett.*, vol. 88, p. 121123, 2006.
[42] G. Scalari, S. Blaser, J. Faist, H. Beere, E. Linfield, D. Ritchie, and G. Davies, "Terahertz emission from quantum cascade lasers in the quantum hall regime: Evidence for many body resonances and localization effects," *Phys. Rev. Lett.*, vol. 93, p. 237403, 2004.
[43] B. S. Williams, S. Kumar, Q. Hu, and J. L. Reno, "High-power terahertz quantum-cascade lasers," *Electron. Lett.*, vol. 42, p. 89, 2006.
[44] H.-W. Hübers, S. G. Pavlov, A. D. Semenov, R. Köhler, L. Mahler, A. Tredicucci, H. E. Beere, D. A. Ritchie, and E. H. Linfield, "Terahertz quantum cascade laser as local oscillator in a heterodyne receiver," *Opt. Exp.*, vol. 13, p. 5890, 2005.
[45] A. Lee, B. S. Williams, S. Kumar, Q. Hu, and J. L. Reno, "Real-time imaging using a 4.3-THz quantum cascade laser and a 320 × 240 microbolometer focal-plane array," *IEEE Photon. Technol. Lett.*, vol. 18, no. 13, p. 1415, Jul. 2006.
[46] J. Darmo, V. Tamosiunas, G. Fasching, J. Kröll, K. Unterrainer, M. Beck, M. Giovannini, J. Faist, C. Kremser, and P. Debbage, "Imaging with a terahertz quantum cascade laser," *Opt. Exp.*, vol. 12, p. 1879, 2004.
[47] M. I. Amanti, M. Fischer, C. Walther, G. Scalari, and J. Faist, "Horn antennas for terahertz quantum cascade lasers," *Electron. Lett.*, vol. 43, p. 573, 2007.
[48] A. W. M. Lee, Q. Qin, S. Kumar, B. S. Williams, Q. Hu, and J. L. Reno, "High-power and high-temperature THz quantum-cascade lasers based on lens-coupled metal-metal waveguides," *Opt. Lett.*, vol. 32, p. 2840, 2007.
[49] E. E. Orlova, J. N. Hovenier, T. O. Klaassen, I. KaŠalynas, A. J. L. Adam, J. R. Gao, T. M. Klapwijk, B. S. Williams, S. Kumar, Q. Hu, and J. L. Reno, "Antenna model for wire lasers," *Phys. Rev. Lett.*, vol. 96, p. 173904, 2006.
[50] D. B. Rutledge, D. P. Neikirk, and D. P. Kasilingam, "Integrated-circuit antennas," in *Infrared and Millimeter-Waves,* vol. 10, K. J. Button, Ed. San Francisco, CA: Academic, 1983, pp. 1–90.
[51] A. J. Fitzgerald, B. E. Cole, and P. F. Taday, "Nondestructive analysis of tablet coating thickness using terahertz pulsed imaging," *J. Pharm. Sci.*, vol. 94, p. 177, 2005.
[52] K. Kawase, "Terahertz imaging for drug detection and large-scale integrated circuit inspection," *Opt. Photon. News*, vol. 15, p. 34, 2004.
[53] J. Chen, Y. Chen, H. Zhao, G. J. Bastiaans, and X. C. Zhang, "Absorption coefficients of selected explosives and related compounds in the range 0.1–2.8 THz," *Opt. Exp.*, vol. 15, p. 12060, 2007.
[54] N. Butler, R. Blackwell, R. Murphy, R. Silva, and C. Marshall, "Dual use, low cost microbolometer imaging system," *Proc. SPIE*, vol. 2552, p. 583, 1995.

Sushil Kumar (M'99) was born in Jaipur, India. He received the B.E. degree from the Delhi College of Engineering, Delhi, India, in 1998, the M.S. degree from the University of Michigan, Ann Arbor, in 2001, and the Ph.D. degree from the Massachusetts Institute of Technology, Cambridge, in 2007, all in electrical engineering.

He is currently a Postdoctoral Associate at the Research Laboratory of Electronics, Massachusetts Institute of Technology. His current research interests include development of terahertz quantum cascade lasers (QCLs) and other devices based on intersubband transitions in quantum-wells.

Alan W. M. Lee (M'00) was born in Guelph, Canada. He received the B.A.Sc. degree from the University of Waterloo, Waterloo, ON, in 2002, and the M.S. degree from the University of California, Los Angeles, in 2004, both in electrical engineering. He is currently working toward the Ph.D. degree in electrical engineering in the Department of Electrical Engineering and Computer Science, Massachusetts Institute of Technology, Cambridge.

His current research interests include real-time imaging with terahertz quantum-cascade lasers (QCLs) and cavity engineering of QCLs for improved radiation and power.